

Effects of zonal flows on ion temperature gradient instability in the scrape-off layer of a field-reversed configuration

X.S. Wei^{1,*} , W.H. Wang¹ , Z. Lin^{1,*} , G.J. Choi¹ , S. Dettrick², C. Lau² , P.F. Liu¹ and T. Tajima^{1,2}

¹ Department of Physics and Astronomy, University of California, Irvine, CA 92697, United States of America

² TAE Technologies, Inc., Foothill Ranch, CA 92610, United States of America

E-mail: xishuow@uci.edu and zhihongl@uci.edu

Received 12 May 2021, revised 7 October 2021

Accepted for publication 15 October 2021

Published 10 November 2021



CrossMark

Abstract

Gyrokinetic simulations of long wavelength ion temperature gradient (ITG) turbulence in the scrape-off layer (SOL) of a field-reversed configuration (FRC) find that zonal flows are nonlinearly generated and are the dominant mechanism for the nonlinear saturation of the ITG instability. After the ITG saturation, zonal flows remain undamped and gradually suppress the turbulent transport to a very low level. In the simulations with collisions, collisional damping gradually reduces zonal flow amplitude to a lower level, which allows finite ITG turbulence intensity and ion heat transport in the SOL. The steady state turbulence intensity and ion heat transport are found to be proportional to the collision frequency. This favorable scaling suggests that minimizing collisions (e.g. increasing temperature, reducing impurity content, etc) and preserving toroidal symmetry could improve plasma confinement in the FRC.

Keywords: zonal flow, field-reversed configuration, ITG mode, turbulent transport

(Some figures may appear in colour only in the online journal)

1. Introduction

A field-reversed configuration (FRC) is a prolate compact toroidal with a purely poloidal magnetic field and consists of two regions: a core region with closed field lines and a scrape-off layer (SOL) region with open field lines [1]. As an attractive fusion reactor concept [2], the FRC has been studied extensively in experiment and theory. In particular, recent FRC experiments at TAE Technologies Inc. have successfully stabilized magnetohydrodynamic (MHD) instabilities by using neutral beam injection, plasma gun, and edge biasing [3–6]. In these high-performance discharges, the plasma confinement is in a steady state transport regime where external heating is

balanced by anomalous transport driven by microscopic fluctuations. Therefore, understanding the turbulent transport is critical to improving the plasma confinement in the FRC.

Doppler backscattering (DBS) measurements show that ion scale wavenumbers dominate the density fluctuation spectrum in the SOL, and that electron-to-ion scale fluctuations dominate in the core where the ion scale turbulence is strongly suppressed [7]. Consistent with these experimental observations, local linear gyrokinetic simulations using the gyrokinetic toroidal code (GTC) [8] find that ion temperature gradient (ITG) mode can be unstable in the SOL with a critical pressure gradient comparable to the experimentally measured threshold, but the ion-scale ITG mode is mostly stable in the core [9–11]. Subsequent global nonlinear simulations using the ANC code [12] find that linear ITG instability first grows in the SOL, and then the turbulence spreads from the SOL to the core, resulting in a steady state spectrum characterized by

* Authors to whom any correspondence should be addressed.

lower amplitude core fluctuations and larger SOL fluctuations consistent with experimental measurements [13]. Finally, nonlinear simulations using the GTC-X code [14] find that equilibrium $E \times B$ flow shear can reduce the ITG instability growth rate, saturation amplitude, and ion heat transport in the SOL by reducing both the turbulence intensity and eddy size [15]. The simulation results suggest that maximizing the radial shear of the Doppler-shifted local mode frequency can effectively suppress the ITG instability and associated transport in the FRC SOL.

Besides the equilibrium $E \times B$ flows, zonal flows [16, 17] generated by the microturbulence have been found to greatly suppress the microturbulence and change the transport scaling in the tokamak [8, 18–20]. Zonal flow dynamics in the FRC and tokamak are expected to have similarities and differences since there is no toroidal magnetic field in the FRC. Regarding the similarities, zonal flows can be generated by Reynolds stress of the microturbulence, suppress the microturbulence, and subject to the damping by a tertiary instability in both the FRC and tokamak. Zonal flow amplitude is usually much higher than that of the long wavelength non-zonal modes because the dielectric constant of the zonal modes is much smaller since electrons do not respond to the zonal modes. Regarding the differences, zonal flows are quickly damped to a small residue by collisionless magnetic pumping effects in the tokamak [21], a process that does not exist in the FRC. Therefore, zonal flows can be expected to have a stronger effect in suppressing the turbulence in the FRC. In particular, the nonlinear upshift of the critical pressure gradient [18] could be much more significant in the FRC, where zonal flows can fully suppress the microturbulence near the linear instability threshold. Furthermore, the collisional damping of zonal flows is mainly due to the friction between trapped and passing particles in the tokamak (i.e. neoclassical effects) [22, 23], but is only due to a weaker classical diffusion in the FRC where the guiding center orbit width is zero. Nonetheless, collisional damping due to classical diffusion is the only zonal flow damping mechanism near the linear instability threshold in the FRC. Finally, the FRC has no magnetic shear and thus does not have the linear toroidal coupling in the formation of the driftwave eigenmode, which induces the coherent generation of zonal flows by the modulational instability in the tokamak [24].

In this work, we have extended the GTC-X simulations [14, 15] to include the zonal flow effects on long wavelength ITG turbulence in the FRC SOL. We have first implemented a modified pitch-angle collision operator to model the classical diffusion and verified the zonal flow damping in the gyrokinetic simulation without the microturbulence. We have then performed a series of nonlinear simulations of the ITG turbulence in the SOL with various collision frequencies. In the collisionless simulation, zonal flows are nonlinearly generated and are the dominant mechanism for the nonlinear saturation of the ITG instability. After the ITG saturation, zonal flows remain undamped because of the axisymmetric equilibrium and gradually suppress the turbulent transport to a very low level. In the simulations with collisions, collisional damping gradually reduces zonal flow amplitude to a lower level,

which allows finite ITG turbulence intensity and ion heat transport in the SOL. The steady state turbulence intensity and ion heat transport are found to be proportional to the collision frequency.

Our simulation results have important implications on the turbulent transport in the FRC SOL. Since collision frequency decreases at higher plasma temperature, zonal flows could be enhanced and turbulent transport reduced as plasma temperature increases, which results in a favorable scaling of energy confinement time with the plasma temperature. A similarly favorable transport scaling has been experimentally observed in the FRC experiments [5] and the NSTX spherical tokamak [25]. Therefore, to improve plasma confinement in the FRC, collisions should be minimized (e.g. higher temperature, lower impurity content, etc) and breaking of the toroidal symmetry (e.g. ripple fields, macroscopic MHD activities, etc) should be avoided.

The paper is organized as follows. In section 2, the physical model is described and a model collision operator is constructed. We verify the collision operator for classical diffusion and zonal flow damping in section 3. In section 4, we study zonal flow generation by ITG turbulence, turbulence regulation by zonal flows, and collisional damping of zonal flows and its effects on turbulent transport. The conclusion and summary are given in section 5.

2. Simulation model

2.1. Gyrokinetic simulation model

The electrostatic gyrokinetic Vlasov–Poisson model [30] is used in the current simulation of the FRC SOL, where the gyrokinetic ordering is valid because of the low ion temperature and the strong magnetic field. The ion dynamics is described by gyrokinetic Vlasov equation in the 5D phase space $(\mathbf{X}, v_{\parallel}, \mu)$,

$$\begin{aligned} \frac{\partial f}{\partial t} + \dot{\mathbf{X}} \frac{\partial f}{\partial \mathbf{X}} + \dot{v}_{\parallel} \frac{\partial f}{\partial v_{\parallel}} - C(f) &= 0, \\ \dot{\mathbf{X}} &= v_{\parallel} \mathbf{b} + \mathbf{v}_E + \mathbf{v}_d, \\ \dot{v}_{\parallel} &= -\frac{1}{m_i} \frac{\mathbf{B}^*}{B_{\parallel}^*} \cdot (Z_i \nabla \bar{\phi} + \mu \nabla B), \end{aligned} \quad (1)$$

where f, Z_i and m_i are ion gyrocenter distribution function, charge, and mass, respectively. \mathbf{X} is gyrocenter position, μ magnetic moment, and v_{\parallel} parallel velocity along the magnetic field line. \mathbf{B} is the equilibrium magnetic field, and $\mathbf{b} = \mathbf{B}/B$ is the unit vector. $\mathbf{B}^* = \mathbf{B} + (B v_{\parallel}/\Omega_c) \nabla \times \mathbf{b}$, where Ω_c is ion cyclotron frequency, and $B_{\parallel}^* = \mathbf{B}^* \cdot \mathbf{b}$. $C(f)$ is the collision operator to describe collisions between ions and impurities. $\bar{\phi}$ is gyroaveraged electrostatic potential at the gyrocenter position, $\bar{\phi}(\mathbf{X}) = 1/2\pi \int d\alpha \int d^3\mathbf{x} \phi(\mathbf{x}) \delta(\mathbf{x} - \boldsymbol{\rho} - \mathbf{X})$, where \mathbf{x} represents particle position, α gyrophase, and $\boldsymbol{\rho} = \mathbf{b} \times \mathbf{v}/\Omega_c$ gyroradius. The \mathbf{v}_E represents $E \times B$ drift velocity, and \mathbf{v}_d magnetic drift velocity,

$$\mathbf{v}_E = \mathbf{b} \times \nabla \bar{\phi} / B_{\parallel}^*,$$

$$\mathbf{v}_d = \frac{1}{Z_i B_{\parallel}^*} \left[m_i v_{\parallel}^2 \mathbf{b} \times (\mathbf{b} \cdot \nabla \mathbf{b}) + \mu \mathbf{b} \times \nabla B \right]. \quad (2)$$

The δf method [26–29] is used to reduce particle noise. The ion distribution function is separated into an equilibrium part f_0 and a perturbed part δf . The equilibrium distribution function satisfies the zeroth-order equation:

$$L_0 f_0 = 0, \quad (3)$$

where L_0 is the zeroth-order propagator $L_0 = \partial/\partial t + (\mathbf{v}_{\parallel} \mathbf{b} + \mathbf{v}_d) \cdot \nabla - \mu/m_i \mathbf{B}^* \cdot \nabla B/B_{\parallel}^* \partial_{v_{\parallel}} - C$. Due to the absence of a toroidal magnetic field in the FRC geometry, the local Maxwellian distribution function is an exact solution to equation (3),

$$f_0 = \frac{n_0}{(2\pi T_i/m_i)^{3/2}} \exp \left[-\frac{m_i v_{\parallel}^2/2 + \mu B}{T_i} \right],$$

where n_0 and T_i are equilibrium density and temperature, respectively, which are functions of flux coordinate ψ only.

The perturbed part of the distribution function $\delta f = f - f_0$ can be solved from the perturbed equation

$$L \delta f = -\delta L f_0, \quad (4)$$

where $\delta L = \mathbf{v}_E \cdot \nabla - Z_i/m_i \mathbf{B}^* \cdot (\nabla \bar{\phi})/B_{\parallel}^* \partial_{v_{\parallel}}$ and $L = \delta L + L_0$. By defining a particle weight $w = \delta f/f$, we can obtain the nonlinear weight equation,

$$\frac{dw}{dt} = -\frac{1}{f} \delta L f_0 = (1-w) \left[-\mathbf{v}_E \cdot \frac{\nabla f}{f_0} \Big|_{v_{\perp}} - Z_i v_{\parallel} \mathbf{b} \cdot \frac{\nabla \bar{\phi}}{T_i} \frac{B}{B_{\parallel}^*} - \frac{1}{T_i} \frac{1}{B_{\parallel}^*} \left(m_i v_{\parallel}^2 \nabla \times \mathbf{b} + \mu \mathbf{b} \times \nabla B \right) \right], \quad (5)$$

where we replace $\nabla f_0|_{\mu}$ by $\nabla f_0|_{v_{\perp}} = \nabla f_0|_{\mu} + \frac{\mu \nabla B}{T_i} f_0$.

The perturbed electrostatic potential can be separated into zonal and non-zonal parts. Define $\phi_{00} = \oint \phi J dl_{\parallel} d\zeta / 2\pi \oint J dl_{\parallel}$ as the flux-surface-averaged or zonal potential, where J is the Jacobian. The non-zonal potential is then $\delta \phi = \phi - \phi_{00}$. The perturbed ion gyrocenter density

$$\bar{n}_i(\mathbf{x}) = \int d^3 \mathbf{v} \int d\alpha / (2\pi) \int \delta f(\mathbf{X}) \delta(\mathbf{X} + \boldsymbol{\rho} - \mathbf{x}) d\mathbf{X} \quad (6)$$

can also be separated into zonal part \bar{n}_{00} and non-zonal part $\delta \bar{n}_i$. We assume that electron response to the non-zonal potential of the ITG turbulence is adiabatic, $\delta n_e = n_0 e \delta \phi / T_e$. Then, we can use the following gyrokinetic Poisson's equation [30, 31] to solve the non-zonal potential

$$\frac{Z_i^2 n_0}{T_i} (\delta \phi - \delta \tilde{\phi}) + \frac{e^2 n_0}{T_e} \delta \phi = Z_i \delta \bar{n}_i, \quad (7)$$

where the left-hand side stands for ion polarization density, and $\delta \tilde{\phi}$ comes from the double gyroaveraging of the potential,

$$\delta \tilde{\phi}(\mathbf{x}) = \frac{1}{n_0} \int d^3 \mathbf{v} \int d\mathbf{X} f_0(\mathbf{X}) \delta \bar{\phi}(\mathbf{X}) \delta(\mathbf{X} + \boldsymbol{\rho} - \mathbf{x}). \quad (8)$$

Since the adiabatic response to the non-zonal potential does not drive a radial particle flux, the electron has no response to the zonal potential. Then the equation for the zonal potential ϕ_{00} becomes,

$$\frac{Z_i^2 n_0}{T_i} (\phi_{00} - \tilde{\phi}_{00}) = Z_i \bar{n}_{00}, \quad (9)$$

where $\tilde{\phi}_{00} = \frac{1}{n_0} \int d^3 \mathbf{v} \int d\mathbf{X} f_0(\mathbf{X}) \bar{\phi}_{00}(\mathbf{X}) \delta(\mathbf{X} + \boldsymbol{\rho} - \mathbf{x})$. Equations (1), (5), (7), and (9) make up a closed system for the electrostatic simulation with the zonal flow.

2.2. Collision operator

In this subsection, we describe a simplified collision operator to recover classical transport in the gyrokinetic simulation, which could damp the zonal flow. A pitch angle scattering operator is used here to model the collisions between thermal ions and impurity particles that can drive a perpendicular particle flux. The pitch-angle collision operator has been implemented in GTC [32]

$$C(f_0) = \nu \frac{1}{2} \frac{\partial}{\partial \xi} \left[(1 - \xi^2) \frac{\partial}{\partial \xi} f_0 \right], \quad (10)$$

where $\xi = v_{\parallel}/v = \cos \theta$ is the cosine function of the pitch angle, and ν is the collision frequency. This operator can be implemented using the interpretation in Shanny *et al*'s work [33], where the pitch angle after the collision is computed in the Monte Carlo form,

$$\xi = \xi_0 \cos \sigma + (1 - \xi_0^2) \sin \sigma \cos \eta, \quad (11)$$

where ξ_0 is the pitch angle before collision, η and σ are two angles describing the change of the velocity direction shown in figure 1. Here, \mathbf{w} and \mathbf{u} are two local basis vectors defined as $\mathbf{w} = \mathbf{v}_0 \times \mathbf{b} / |\mathbf{v}_0|$, and $\mathbf{u} = \mathbf{b} \times \mathbf{w}$. σ is the angle between \mathbf{v}_0 and \mathbf{v} , i.e. the change of velocity directions before and after the collision. η is the angle between $\mathbf{v}-\mathbf{v}_0$ plane and $\mathbf{v}_0-\mathbf{b}$ plane. For a small pitch angle scattering, η is randomly chosen between 0 and 2π , i.e. $P(\eta) = 1/2\pi$. The σ is chosen to satisfy the Gaussian distribution,

$$P(\sigma) = \frac{\sigma}{\nu \Delta t} \exp \left(-\frac{\sigma^2}{2\nu \Delta t} \right), \quad (12)$$

where Δt is the time step of each collision.

The classical transport arises from guiding center position change due to the change of particle velocity direction by collisions. Since particle position is unchanged during the collision, the change of guiding center position due to the collision can be calculated,

$$\Delta \mathbf{X} = \frac{\Delta \mathbf{v} \times \mathbf{b}}{\Omega_{ci}}, \quad \Delta \mathbf{v} = \mathbf{v} - \mathbf{v}_0, \quad (13)$$

where $\Delta \mathbf{v}$ is the change of the velocity vector, and $\Delta \mathbf{X}$ is the change of the guiding center position.

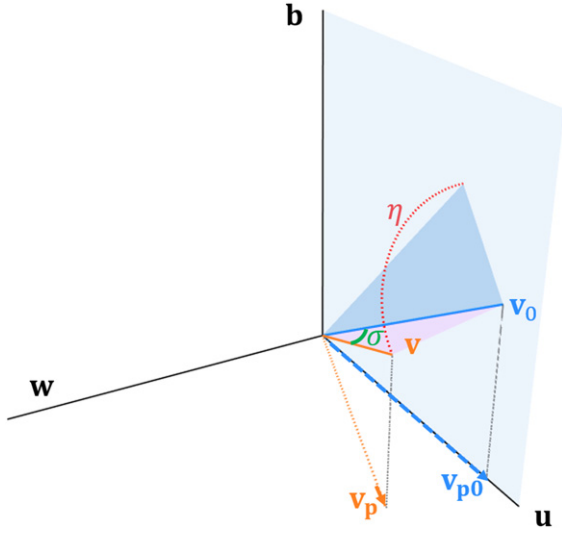


Figure 1. Change of particle velocity due to collision. \mathbf{b} is the unit vector in the direction of the magnetic field. \mathbf{v}_0 and \mathbf{v} are velocity vectors before and after the collision, respectively. \mathbf{v}_{p0} and \mathbf{v}_p are the projections of velocities on \mathbf{w} - \mathbf{u} plane.

After we generate the σ and η angles, we can express the velocity change in the local $(\mathbf{b}, \mathbf{w}, \mathbf{u})$ coordinates,

$$\begin{aligned}\Delta v_b &= (v_0 \cos \sigma - v_0) \cos \theta + v_0 \sin \sigma \cos \eta \sin \theta, \\ \Delta v_u &= (v_0 \cos \sigma - v_0) \sin \theta - v_0 \sin \sigma \cos \eta \cos \theta, \\ \Delta v_w &= v_0 \sin \sigma \sin \eta.\end{aligned}\quad (14)$$

Then we can consider the velocity change in the global coordinates $(\mathbf{b}, \psi, \zeta)$, where ζ is the basis vector in the toroidal direction and $\psi = \zeta \times \mathbf{b}$ is the unit vector perpendicular to the flux surface. In the gyrokinetic simulation, we do not have the information of particle gyrophase angle. Without loss of generality, the gyrophase α can be defined as the angle between \mathbf{u} and ζ , and we assign a random value between 0 to 2π for each particle at each time step. The velocity change in the global coordinate system is given by

$$\begin{aligned}\Delta v_b &= (v_0 \cos \sigma - v_0) \cos \theta + v_0 \sin \sigma \cos \eta \sin \theta, \\ \Delta v_\psi &= \Delta v_u \sin \alpha + \Delta v_w \cos \alpha, \\ \Delta v_\zeta &= \Delta v_u \cos \alpha - \Delta v_w \sin \alpha.\end{aligned}\quad (15)$$

The subsequent calculations of the velocity components in the R and Z directions are straightforward. Thanks to the toroidal symmetry, we only need to calculate the guiding center position change on the R - Z plane, $\Delta R = \Delta \mathbf{X} \cdot \hat{e}_R$, $\Delta Z = \Delta \mathbf{X} \cdot \hat{e}_z$. Correspondingly, the guiding center flux induced by the collisions can be obtained by integrating the effective drift velocity $\mathbf{v}_{\text{col}} = \Delta \mathbf{X} / \Delta t$. This procedure introduces a guiding center random walk on the order of ρ_i in real space.

Note that this collision operator conserves particle number and kinetic energy, but not momentum. We assume that the loss of thermal ion momentum is compensated by impurities or neutral particles, which are presumed not interacting with the

ITG turbulence. The guiding center flux induced by the collision and the associated damping of the zonal flow are verified in section 3. However, the guiding center flux can be removed when calculating the ITG turbulent transport in section 4.

2.3. Simulation settings

Previous studies show that the ion-scale turbulence is mainly driven by the ITG instability in the FRC SOL, which nonlinearly spreads to the core region [12, 13]. For simplicity, the current simulations of the effects of zonal flows on the long wavelength ITG instability are carried out only in the SOL. If not specially mentioned, the simulation region is chosen as $Z \in [-9.37R_0, 9.37R_0]$ of the confinement vessel with a periodic boundary in the axial direction, and the poloidal flux function ψ ranges from $\psi(R = 1.7R_0, Z = 0)$ to $\psi(R = 2.4R_0, Z = 0)$, which is restricted in the SOL region where the most unstable ITG mode locates. Here $R_0 = 0.269$ m is the major radius of the magnetic axis. The simulation domain on the R - Z plane is shown in figure 2. This equilibrium field is constructed using a 2D axisymmetric LR_eqMI equilibrium code [34]. The ion equilibrium profiles used in the simulation is given independently from analytic formulations, with the density profile $n(\psi) = n_0 \left[1 + C_{n1} \left(\tanh \frac{C_{n2} - \psi}{C_{n3}} - 1 \right) \right]$, and the temperature profile $T(\psi) = T_0 \left[1 + C_{T1} \left(\tanh \frac{C_{T2} - \psi}{C_{T3}} - 1 \right) \right]$. The corresponding coefficients are $n_0 = 0.75$, $C_{n1} = 0.409$, $C_{n2} = 0.65$, $C_{n3} = 0.899$, $T_0 = 1$, $C_{T1} = 0.177$, $C_{T2} = 0.95$, and $C_{T3} = 0.718$. Here, the flux function ψ is normalized by $\psi_{\text{unit}} = B_0 R_0^2$, where $B_0 = 531$ G and $R_0 = 0.269$ m. The equilibrium profiles are shown in figure 3. Previous study [14] with the same equilibrium magnetic field and similar ion profile shows $\rho_i / R_0 \ll 1$ and $\omega / \Omega_c \ll 1$, which verifies the validity of gyrokinetic model for the FRC SOL. The coefficients are chosen such that the gradients ∇n_i and ∇T_i have a maximum around $R = 1.9R_0$. The density and temperature are normalized by $n_{e0} = 2.44 \times 10^{13} \text{ cm}^{-3}$, and $T_{e0} = 80$ eV. The electron has the same density profile as the ion, and electron temperature is uniform $T_e = T_{e0}$. The corresponding ion beta at the outer mid-plane is also shown in figure 3. The experimental data shows that $\beta_i \approx 0.027$ on the reference surface ($R = 1.9R_0$, $Z = 0$). While this finite beta value can have stabilizing effects on the ITG instability, density fluctuations on the ion gyroradius scale has been observed by the DBS measurements in the SOL of the C-2 FRC experiments [7]. We also note that this beta value of 2.7% in the FRC SOL is in the range of the beta value in high performance tokamak plasmas, where the ITG instability is commonly observed and simulated. Besides the stabilizing effects on the ITG instability, the finite beta effects can reduce the effectiveness for the generation of the zonal flows by the microturbulence through partial cancellation between Reynolds stress and Maxwell stress, especially for the Alfvénic fluctuations [19]. However, this finite beta effects on the zonal flow generation is less important for the acoustic fluctuations driven by the ITG instability. Nonetheless, it is important to incorporate the finite beta effects in the future study of the ITG instability and

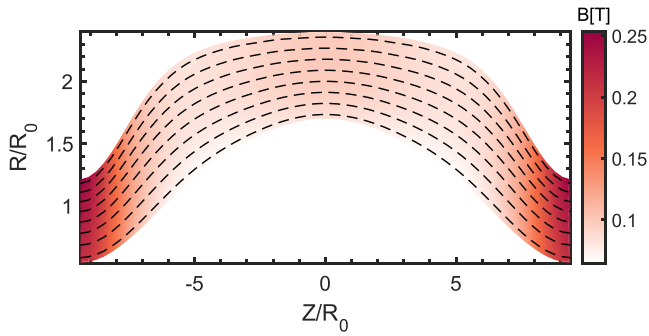


Figure 2. Simulation domain in FRC SOL. Black dash lines are magnetic field lines. Colors represent magnetic field magnitude B .

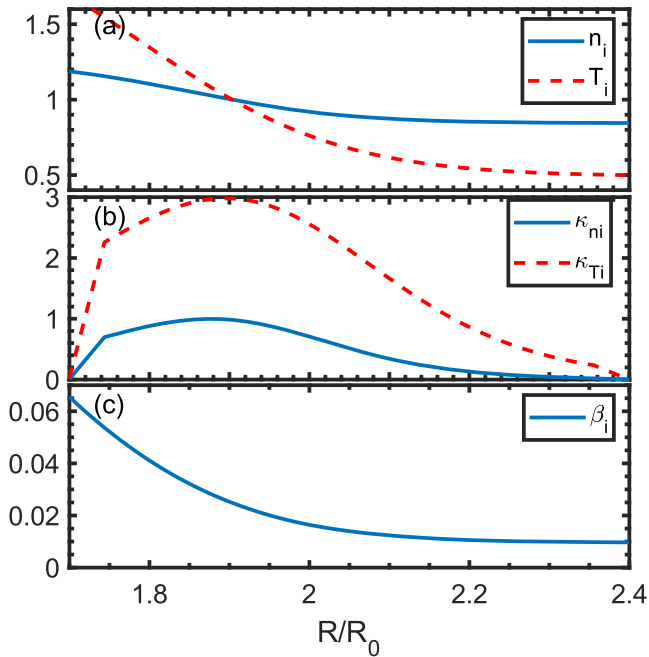


Figure 3. Radial profiles of ion density and temperature (panel (a)) and their gradients $\kappa_{n,T}$ (panel (b)). The ion beta $\beta = 2\mu_0 P_i / B^2$ at mid-plane is shown in (panel (c)). Density and temperature are normalized by their values at $R = 1.90R_0$ and $Z = 0$.

zonal flow generation in the FRC SOL. In the current work, we only focus on electrostatic turbulence in the SOL. In the simulations we use the uniform loading method, where we keep the physical gradients, but force the marker particle n_0 and T_i to equal to the value at a certain flux surface [35]. In that way, we can exclude the collisional equilibrium radial flux and only focus on the turbulent transport.

In all simulations, only one toroidal mode with $n = 20$ is kept. All parallel harmonics are kept. An efficient gyroaveraging method has been implemented for the single- n mode simulation. The new gyroaveraging method uses the Bessel function for the toroidal gyroaveraging. In the R - Z plane, two points are selected in the direction perpendicular to the magnetic field for the radial gyroaveraging. In the end, we have $\bar{\phi}(\mathbf{X}) = \frac{1}{2}J_0(k_\zeta \rho) [\phi(\mathbf{X} + \Delta\mathbf{x}) + \phi(\mathbf{X} - \Delta\mathbf{x})]$, where $k_\zeta = n/R$ is the toroidal wave number, and $\Delta\mathbf{x}$ is

the effective gyroradius vector on the R - Z plane and perpendicular to the field line, with the length $|\Delta\mathbf{x}| = \rho/\sqrt{2}$. We have demonstrated that this method achieves the same accuracy as the conventional four-point averaging method while avoiding inefficient toroidal MPI communication for the FRC simulations [15].

3. Verification of collisional damping of zonal flow

Zonal flows in the FRC can be damped by ion guiding center flux induced by the Coulomb collisions (i.e. classical transport) with impurities or neutrals. In this section, we verify this collisional damping of the zonal flows using the model pitch-angle collision operator formulated in section 2.2. The radial particle flux resulting from the guiding center random walk due to the pitch-angle scattering is expected to obey the Fick's Law, $\Gamma = -\mathbf{D} \cdot \nabla n$, where $\mathbf{D} = \langle \Delta\mathbf{X}\Delta\mathbf{X} \rangle / (2\Delta t)$. A full- f simulation without turbulence is carried out for this verification. We initiate a non-uniform guiding center profile. The guiding center motion is calculated from equation (1), where $\bar{\phi}$ is set to be 0. The radial guiding center flux can be calculated by integrating the effective radial drift velocity $\mathbf{v}_{\text{col}} = \Delta\mathbf{X}/\Delta t$ due to the collisions from equation (13). We can also calculate the diffusivity \mathbf{D} theoretically and obtain a 'theoretical' guiding center flux using density gradient ∇n measured from the simulation.

The parallel simulation domain is chosen as $Z \in [-0.1R_0, 0.1R_0]$ to minimize variations of equilibrium geometry in the z -direction, and the radial domain is the same as figure 2. For simplicity, we use a constant collision frequency in equation (13). The initial guiding center profile is loaded as $n_{\text{init}} = n_{e0} \{1 + 0.25 \times \tanh[(1.7 - \psi)/0.5] - 1\}$, and a uniform temperature profile $T_{\text{init}} = T_{e0}$ is used with a Maxwellian distribution function. The collision frequency is set as $\nu = 30C_s/R_0$. Figure 4 shows the radial profiles of the guiding center density and fluxes. In figure 4(a), the initial profile of the density profile is relaxed due to the radial diffusion after about three collision times. For this verification, we initiate particle velocity perpendicular to \mathbf{b} and only consider the gyro-phase change due to the pitch-angle scattering. Note that in simulation the effective radial velocity of the guiding center flux due to collisions $v_{\text{col},R} = \mathbf{v}_{\text{col}} \cdot \nabla R$ must be evaluated in the position after collision, while the basis vectors in equation (15) are evaluated in the position before each collision. The radial diffusion can be calculated from equations (12) and (14), which gives rise to a mean square of guiding center excursion $\langle \Delta R^2 \rangle = 3\rho_i^2 \nu \Delta t$ and the associated classical transport with a diffusivity of $D_R = 3\rho_i^2 \nu / 2$, where ρ_i is the gyroradius of ions with thermal speed. Using this diffusivity, the guiding center flux calculated from the Fick's law is compared to that measured from simulations in figure 4(b), and the two methods show good agreement. This verifies that the collision operator is implemented correctly. The calculated radial heat flux is 0 because the initial temperature is uniform.

Now we can verify the collisional zonal flow damping due to the classical transport induced by the model pitch-angle scattering. In order to verify the simulation results by

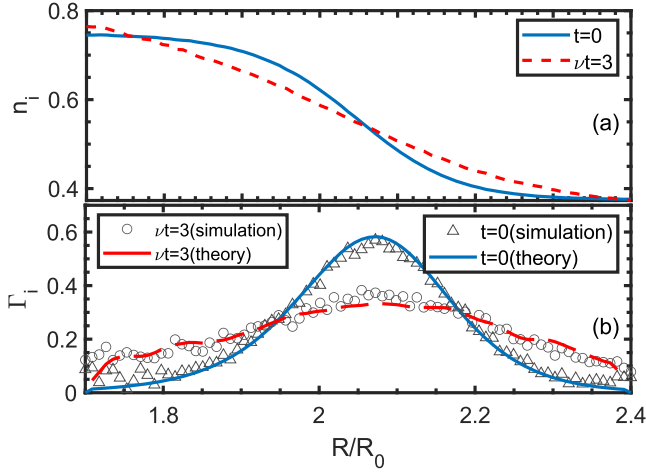


Figure 4. Radial profiles of density n_i (panel (a)) and guiding center flux Γ_i (panel (b)) at $t = 0$ and at $\nu t = 3$. Theoretical guiding center fluxes are compared with simulation results in (panel (b)). Density is normalized by n_{e0} and guiding center flux is normalized by $n(R) v_{th}$.

the analytic theory, we first simulate the collisional damping of the zonal flow with a single radial wavelength and in the absence of the ITG turbulence. We select a particular zonal flow radial wavelength by limiting the simulation domain in the radial direction and keeping the same narrow domain in the z -direction, i.e. $Z \in [-0.1R_0, 0.1R_0]$ and ψ ranges from $\psi(R = 1.97R_0, Z = 0)$ to $\psi(R = 2.04R_0, Z = 0)$. Using the δf simulation method, we initiate a zonal flow perturbation $\delta f = 0.1 \sin [4\pi(R - R_{in}) / (R_{out} - R_{in})] f_0$, where R_{in} and R_{out} are the major radius at inner and outer boundaries. The diffusion equation describing the evolution of δf is given by

$$\frac{\partial \delta f}{\partial t} = \frac{1}{2} \frac{\partial^2 \delta f}{\partial R^2} \frac{\Delta R_v^2}{\Delta t}, \quad (16)$$

where ΔR_v^2 is defined as the radial excursion for particles with a certain velocity and can be evaluated from equations (12) and (13)

$$\Delta R_v^2 = \int \left(\frac{\Delta \mathbf{v} \times \mathbf{b}}{\Omega_c} \cdot \nabla R \right)^2 \frac{d\eta}{2\pi} P(\sigma) d\sigma \frac{d\alpha}{2\pi} = \rho^2 \nu \Delta t, \quad (17)$$

where $\rho = v/\Omega_c$. The initial perturbed guiding center density is given as $\delta f_{init} = \delta n_0 (2\pi v_{th}^2)^{-3/2} \exp(-v^2/(2v_{th}^2))$. The solution of equation (16) is $\delta f(t) = \delta f_{init} \exp(-k_r^2 \rho^2 \nu t/2)$. The guiding center radial excursion $\langle \Delta R^2 \rangle$ averaged over particle velocity is given by

$$\langle \Delta R^2(t) \rangle = \frac{\int \delta f \Delta R_v^2 dv}{\int \delta f dv} = \nu \Delta t \frac{3\rho_i^2}{1 + k_r^2 \rho_i^2 \nu t}. \quad (18)$$

The radial excursion is proportional to the square of particle velocity. As a result, the population of particles at a certain radial location with different velocities will evolve with time, which means the velocity distribution will deviate from the initial function. This effect is reflected in the ν dependence in the exponential decay factor of δf , and in the time-dependence

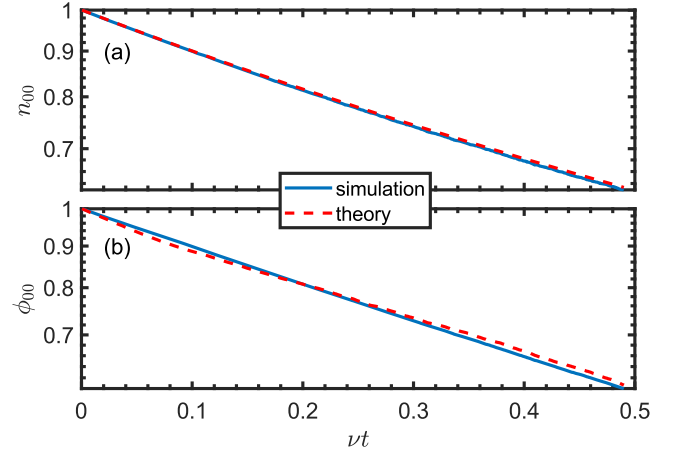


Figure 5. Time history from simulation for density (panel (a)) and zonal potential (panel (b)) at $R = 1.995R_0$. Both quantities are normalized by their initial values.

factor in the denominator in equation (18). The radial guiding center flux driven by the perturbed zonal density gradient can be estimated by $\Gamma_R = -(\partial_R \delta n) \langle \Delta R^2 \rangle / (2\Delta t)$. Figure 5 shows the evolution of perturbed density and zonal potential at a certain radial position $R = 1.995R_0$. The damping is nearly exponential with a deviation arising from the extra time-dependence of $\langle \Delta R^2 \rangle$. Figure 5(a) shows an excellent agreement between simulation and theory for the damping of zonal density perturbation. In figure 5(b), the zonal potential is solved by equation (9) in real space using the Padé approximation [31]. Figure 5(b) shows that the evolution of the zonal potential from simulation and our model agrees well.

So far we verify the collisional damping of the zonal flows by comparing simulation results with the analytic theory in a small simulation domain to avoid the complication of equilibrium geometry. We now perform more realistic simulations in a larger domain to incorporate variations of the equilibrium geometry and a physical collision frequency in the FRC SOL. In this simulation, the parallel simulation domain is in the range of $(-9.37R_0, 9.37R_0)$, so that the passing and trapped particles co-exist due to the non-uniformity of the B field. We limit the radial domain from $\psi(R = 1.97R_0, Z = 0)$ to $\psi(R = 2.04R_0, Z = 0)$ such that we can select a radial wavevector k_r of the zonal potential. The collision frequency in the simulation region is almost constant $\nu \approx 0.061 C_s/R_0$. The zonal flow damping in figure 6 shows nearly exponential damping of the zonal flows during a short simulation time when the extra time-dependent term in the $\langle \Delta R^2 \rangle$ can be ignored. The damping rate is proportional to the k_r^2 , as expected. In the longer time simulation, the damping rate slowly decreases and no longer scales with the k_r^2 because the distribution function changes with the time and the $\langle \Delta R^2 \rangle$ is no longer proportional to ρ_i^2 . The dependence of the initial damping rate on the k_r^2 verifies that the collisional zonal flow damping is through classical viscosity, rather than friction between trapped and passing particles as in the tokamak.

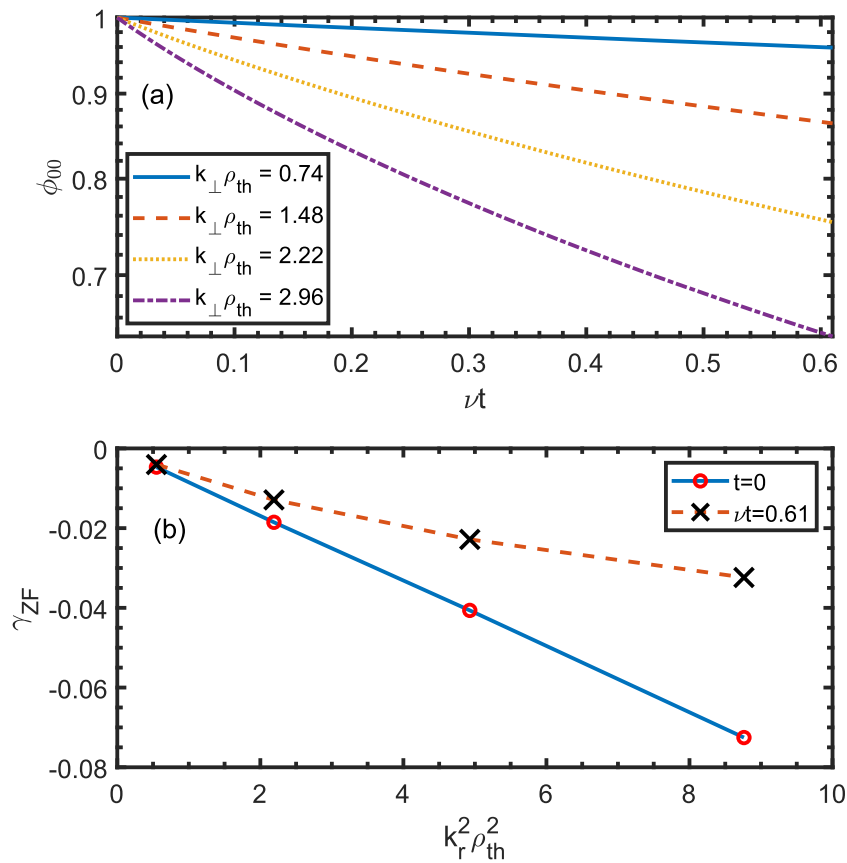


Figure 6. Time history of zonal flows with different radial wavelength (panel (a)) and damping rate dependence on k_r^2 (panel (b)). Potential is normalized by its initial value. The damping rate is normalized by C_s/R_0 .

4. Zonal flow effects on ITG turbulence in FRC SOL

4.1. Zonal flows driven by ITG instability in FRC SOL

In this subsection, we study the zonal flow driven by long wavelength ITG instability in the FRC SOL in the collisionless limit. To focus on the basic physics of zonal flow generation and its effects on the ITG turbulence, we simulate the single toroidal mode $n = 20$ of the ITG instability and the zonal mode of $n = 0$. The motivation for simulating a single- n ITG is based on the insights from previous tokamak study, which shows that the nonlinear coupling between a single toroidal mode with the zonal mode dominates the ITG nonlinear dynamics, while the couplings between multiple toroidal modes are subdominant [24]. Nonetheless, multiple unstable toroidal modes can simultaneously drive zonal flows and modify the radial structure of the zonal flows, which is important for the suppression of turbulence [19]. We choose the $n = 20$ mode since it is the nonlinearly dominant mode due to the inverse cascade in the simulation without zonal flows [13]. In the multi-mode simulation [13], the $n = 20$ mode first grows exponentially with its own linear growth rate in the early linear phase, but is mostly generated by the linearly most unstable modes closer to the nonlinear saturation phase. Nonetheless, the basic physics of zonal flow generation in this simulation of the $n = 20$ mode is applicable to the linearly most unstable modes in the multi-mode simulation. The nonlinear stage of the single- n ITG is still

turbulence because of the nonlinear interactions between all poloidal and radial harmonics and the parallel wave-particle decorrelation that drives the turbulent transport [15]. A model heat bath is applied in the simulation to fix the temperature profile in order to avoid the quasi-linear relaxation due to the turbulent transport [15, 36]. In the future study, we will simulate nonlinear couplings of multiple n -modes [13] together with zonal flows for a more realistic assessment of the turbulent transport in the SOL.

The radial domain ranges from $\psi(R = 1.7R_0, Z = 0)$ to $\psi(R = 2.4R_0, Z = 0)$ for all ITG simulations reported in this section. The mode amplitude peaks at the surface of $\psi(R = 1.9R_0, Z = 0)$, where $\rho_i/R_0 \approx 0.050$, and $k_{\zeta} \rho_i \approx 0.53$ at the outer mid-plane. The time evolution of the root-mean-square of the non-zonal potential and zonal potential is plotted in figure 7. For comparison, another simulation is carried out in which only passively generated zonal flow is measured. The term ‘passively generated’ means that the zonal flow is generated through nonlinear couplings of the ITG modes, but the zonal flow has no feedback to the ITG modes, i.e. the guiding center motion does not include the $E \times B$ drift of the zonal electric field. Figure 7(a) shows that the turbulence amplitude after saturation ($t > 70 R_0/C_s$) is significantly suppressed by the zonal flow. In the stage before saturation ($t < 70 R_0/C_s$), the zonal flow is mainly driven by nonlinear mode coupling rather than modulational instability, since the zonal flow growth rate $\gamma_{ZF} \approx 2\gamma_{ITG}$ is not sensitive to the

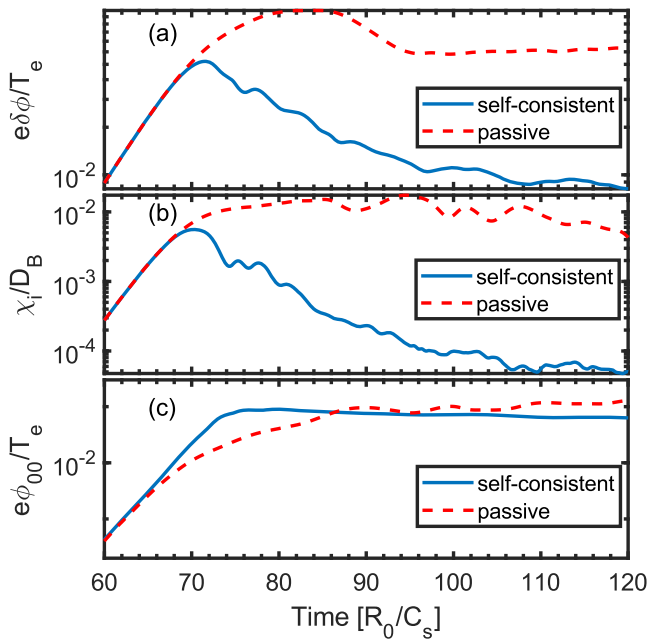


Figure 7. Time history of non-zonal (panel (a)) and zonal (panel (b)) mode amplitudes, and the volume averaged ion radial heat conductivity (panel (c)). Both quantities are averaged over the whole simulation volume.

non-zonal mode intensity. The passively generated zonal flow no longer grows exponentially after the ITG instability saturates at $t \sim 85 R_0/C_s$. The ITG turbulence and the zonal flow then reach a quasi-steady state with a high transport level in the SOL. The zonal flow saturation amplitude between passive generated and self-consistent cases are similar, which indicates the nonlinear damping of the zonal flow is weak in this collisionless simulation, where the non-zonal mode intensity is low in the nonlinear stage. The zonal flow amplitude slightly decreases after the nonlinear saturation in the self-consistent case. However, the rate of this decrease is much smaller than the zonal flow growth rate in the linear phase and diminishes as the ITG amplitude decreases. Note that the zonal flow in the FRC has no collisionless damping through the magnetic pumping as in the tokamak [21]. The radial structure of the zonal flows does not evolve in time, so the time history of the zonal flow amplitude shows in figure 7 is very similar to that of the zonal flow $E \times B$ drift velocity and the associated shearing rate.

4.2. Zonal flow regulation on ITG turbulence in FRC SOL

In the previous study, we have shown that the long wavelength ITG instability in the SOL can saturate due to fluid eddy rotation in the radial-toroidal plane, even in the absence of zonal flow. [15] In figure 7 the ITG instability in self-consistent simulation saturates when the zonal and non-zonal component is comparable ($t \sim 70 R_0/C_s$). Comparing with the case without zonal flow, the ITG instability in self-consistent simulation shows earlier saturation time and lower saturation amplitude, which suggests that zonal flow is the dominant saturation

Table 1. Characteristic frequencies. All quantities are evaluated at ($R = 1.9R_0, Z = 0$). The frequency unit is C_s/R_0 .

$ \omega_{\text{ITG}} $	0.6
$ \omega^* $	0.5
$k_{\parallel} C_s$	0.3
$ \omega_c $	0.16

mechanism for the long wavelength ITG instability in the FRC SOL. After saturation, the non-zonal component drops quickly to a low level. Because zonal flow is undamped in the nonlinear stage the non-zonal fluctuation and heat diffusivity continue to decrease, which indicates that there is no steady state ion heat transport in the absence of the zonal flow damping. This indicates that the ITG turbulence intensity and ion heat transport can be non-zero only with a pressure gradient much higher than the linear threshold, which is similar to the so-called Dimitis' shift in the tokamak [18].

In table 1, we list the linear frequency of ITG instability ω_{ITG} , the drift wave frequency $\omega^* = k_{\parallel} T_e / (eBL_m)$, the ion acoustic wave frequency $k_{\parallel} C_s$, and the averaged curvature drift frequency $\omega_c = k_{\perp} v_i^2 \nabla \times \mathbf{b}_0 / \Omega_{ci}$. The ω_{ITG} is closer to ω^* than the ω_c , which suggests that the ITG mode found in the FRC SOL is a mixture of the slab branch and the toroidal branch. Comparing figure 7(c) with previous zonal flow simulations in the tokamak (e.g. figure 1 in [8]), we can see that the zonal flow effect on initial ITG saturation in the FRC SOL is not as strong as that in the tokamak. This is consistent with earlier studies showing that the effect of zonal flow at the ITG saturation is generally stronger for the toroidal ITG [37] than the slab-like ITG [20, 38]. However, the effects of zonal flows can depend on various plasma parameters and the nature of primary instability. More importantly, the zonal flow dynamics after the nonlinear saturation (e.g. collisionless damping) can depend sensitively on the magnetic geometry. Nonetheless, the zonal flow effect in the FRC SOL is still important because there is no efficient zonal flow damping mechanism. The undamped zonal flow has a large amplitude and continuously suppresses the ITG turbulence.

In figure 8 we show the non-zonal potential in the radial-toroidal plane. The three columns of figure 8 correspond to the linear stage ($t = 60 R_0/C_s$), the saturation stage ($t = 80 R_0/C_s$), and the nonlinear stage ($t = 110 R_0/C_s$). In the linear stage, the mode locates at the strongest temperature gradient region. In the nonlinear stage without the zonal flow (first row of figure 8), the shape of the mode in structure persists with the eddies moving slightly outward. When the zonal flow is included (second row of figure 8), the mode structure is distorted by the zonal flow shear after the saturation. The mode structure breaks into even smaller eddies in the late nonlinear stage. A broader k_r spectrum is observed after the saturation, as shown in figure 9. This diffusion in the k_r space is due to the zonal flow random shearing, which leads to the reduction of the turbulence and transport level [39]. Zonal flow also has effects on the turbulence spreading, as can be seen from the eddy location and size in figure 8.

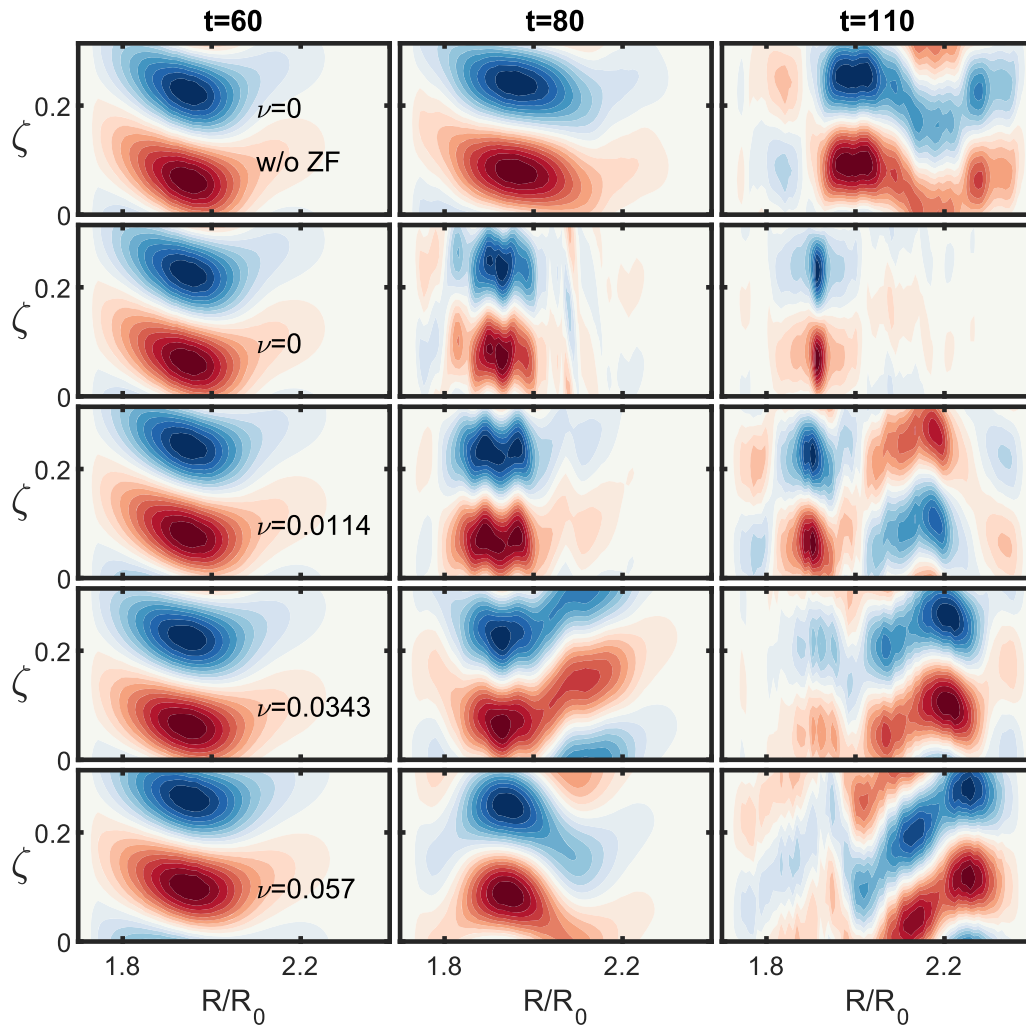


Figure 8. Non-zonal mode structure on R - ζ plane from simulations with various collision frequencies. Three columns correspond to linear, saturation, and nonlinear stages. $1/20$ of the torus ($0 < \zeta < \pi/10$) is shown.

4.3. Collisional effects on zonal flow and turbulence

As discussed in section 3, zonal flow can be damped by collisions, which can maintain a steady state turbulent transport. We carry out simulations with different collision frequencies, with ν ranging from 0 to $0.057 C_s/R_0$ (about $\gamma_{ITG}/3$), where the $\nu = 0$ case is identical to the collisionless simulation described in sections 4.1 and 4.2. Since ion-ion like-species collisions do not induce a radial particle flux, the zonal flow damping comes from the collision of the ions with impurities and neutrals. There is no experimental data to calculate the frequency of the ion collisions with impurities and neutrals. As a reference, the ion-ion collision frequency is $\nu \sim 0.0114 C_s/R_0$ using ion density and temperature at the reference surface of $R = 1.9R_0$ as shown in figure 3. Figure 10 shows the comparison between turbulent transport and collision-induced particle mobility when $\nu = 0.057 C_s/R_0$. The mobility measuring the amplitude of the radial random motion induced by the collision is found to be much smaller than the ion heat conductivity which measures the amplitude of the radial random motion due to the turbulence $E \times B$ drifts. In the nonlinear stage, a quasi-steady state turbulence is maintained by a balance between the

linear ITG drive and the turbulence suppression by the zonal flows. The zonal flows are in a quasi-steady state due to the balance between zonal flow generation by the turbulence and the collisional damping of zonal flows. Figure 10 illustrates that the turbulent transport is still the dominant heat transport mechanism after the inclusion of collisions.

The scaling of linear and nonlinear properties with different collision frequencies can be found in figure 11. The collisional effect on the ITG linear growth rate is negligible as shown in figure 11(a). The non-zonal mode intensity in the nonlinear stage increases with collision frequency as shown in figure 11(b). When $\nu \approx \gamma_{ITG}/3$, the non-zonal mode amplitude increases by a factor of 2. The zonal flow amplitude decreases with collisions and therefore the turbulent transport is enhanced. Figure 11(c) shows the volume and time-averaged ion heat conductivity χ_i , which increases by a factor of 10 when $\nu \approx \gamma_{ITG}/3$. Figure 11(d) shows the volume averaged zonal flow shearing rate in the nonlinear stage, where the local shearing rate is defined as $\omega_s = R^2 B \partial^2 \langle \phi \rangle / \partial^2 \psi$ by assuming isotropic eddies. In the collisionless simulation, $\omega_s > \gamma_{ITG}$ when the mode saturates at $t \sim 70R_0/C_s$. In the nonlinear stage, $\omega_s \sim 3\gamma_{ITG}$, which again indicates that the zonal flow

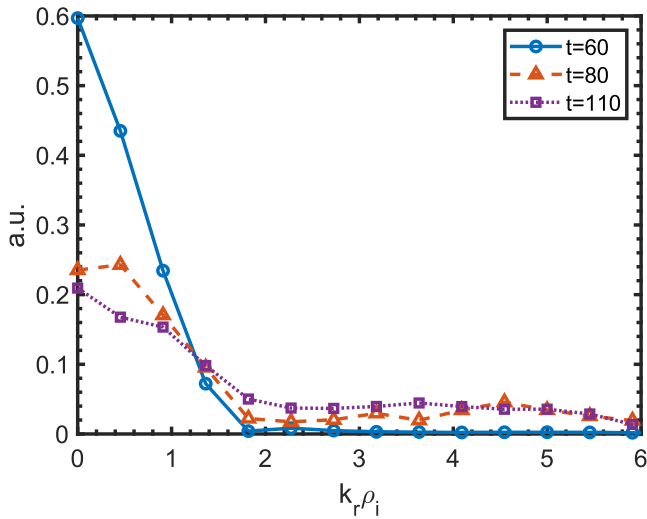


Figure 9. Radial fluctuation spectrum at the mid-plane from collisionless simulation with the zonal flow. These three lines correspond to the three plots in the second row of figure 8. The amplitude of each line is normalized by the total spectrum intensity.

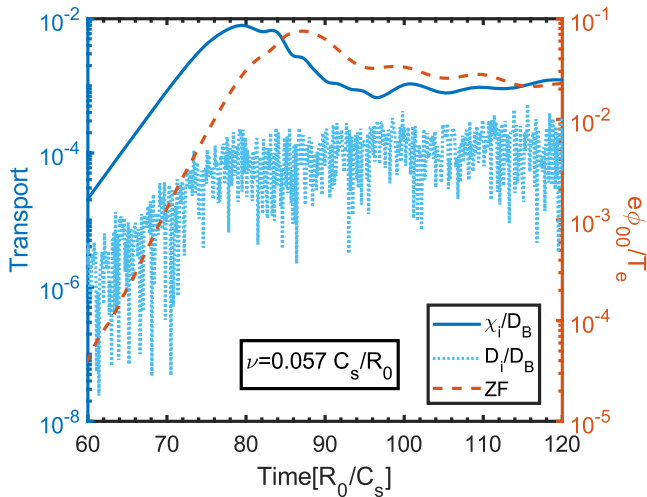


Figure 10. Time history of ion heat conductivity χ_i (dark blue) driven by ITG turbulence and ion mobility (light blue) induced by collision. The two quantities are normalized to Bohm unit $D_B = T_{e0}/eB_0$. The associated volume averaged ZF amplitude (orange) is also shown.

shearing is the dominant saturation mechanism for the long wavelength ITG instability in the FRC SOL. For simulations with collisions, the zonal flow shearing rate is lower, which leads to higher turbulence intensity and transport level. Note that there is no geodesic acoustic mode oscillation in the FRC and the nonlinear effects on the zonal flow evolution are weak. So the zonal flow amplitude reaches a steady state after saturation and the shearing rate is almost time static. Although the collisions introduce slow oscillations on zonal flow after saturation, the oscillation frequency is much smaller than the shearing rate itself. Therefore, there is no reduction in the

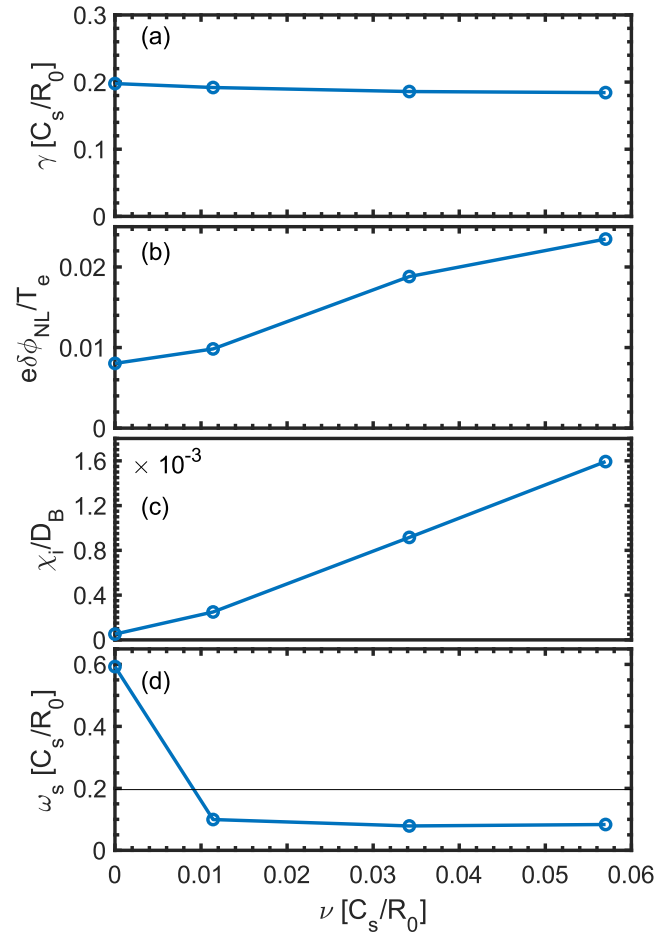


Figure 11. Dependence on collision frequencies for ITG linear growth rate (panel (a)), non-zonal mode amplitude in nonlinear (NL) stage (panel (b)), heat conductivity (panel (c)), and zonal flow shearing rate (panel (d)). In (b)–(d) the quantities are RMS values averaged between $t = 100R_0/C_s$ and $t = 120R_0/C_s$. In (d) horizontal black line is the linear ITG growth rate.

effective zonal flow shearing due to the finite zonal flow frequency [39]. Apart from the enhancement of radial transport, collisional damping of the zonal flow can also enhance the turbulence spreading in the radial direction as shown in figure 8. The turbulence spreading shown in figure 8 is mainly toward the larger R region since the linear instability peaks at the inner boundary of the simulation domain because of the pressure profile used in the current simulations. In general the turbulence spreads in both radial direction and can reach the stable core region [13]. The lower three rows of figure 8 show that the more coherent mode structure after saturation is restored by including collisions. In the nonlinear stage, the eddies are again expanding in the radial direction due to the turbulence spreading. The finding that zonal flow amplitude and turbulence intensity depend on the collision frequency is consistent with the notion that dissipation plays an important role in the self-organization of the turbulence [24] and zonal flow generation [40].

5. Conclusion and future work

In this work, we have studied the zonal flow effects on ITG turbulent transport in the FRC SOL using the particle simulation code GTC-X. A model collision operator incorporating changes of guiding center positions due to pitch-angle scattering has been implemented and verified to recover classical transport and zonal flow damping. The dominant mechanism of zonal flow damping in the FRC is classical diffusion (or viscosity) resulting in a damping rate proportional to the square of the zonal flow radial wavenumber k_r^2 .

A series of nonlinear simulations have been performed for the long wavelength ITG turbulence in the FRC SOL. Zonal flows are shown to be generated mainly by nonlinear mode coupling rather than modulational instability, with a growth rate $\gamma_{ZF} \approx 2\gamma_{ITG}$ and not sensitive to the ITG mode amplitude. Zonal flows are the main saturation mechanism for the long wavelength ITG instability. The zonal flow shearing rate exceeds the ITG linear growth rate when the ITG instability saturates, and the radial correlation length and eddy size of the ITG turbulence is reduced by the zonal flows. In the collisionless limit, the zonal flows remain undamped in the nonlinear stage and eventually suppress the ITG turbulence to a very low level. As a result, the radial ion heat conductivity and turbulence spreading are strongly suppressed. The collisions can damp the zonal flows and enhance the turbulent transport in the FRC SOL. With collisional damping, the zonal flow shearing rate can be comparable to or smaller than γ_{ITG} after the saturation of the ITG instability, which leads to a much larger ion heat conductivity, radial eddy size, and radial turbulence spreading.

In the future FRC studies, we will incorporate more physics in the simulations including drift kinetic electrons and fully kinetic ions. We will scan the parameter space to find the possible tertiary instability of the zonal flows, which extracts energy from zonal flows and results in finite turbulence co-existing with the zonal flows. We will also study couplings between parallel and perpendicular transport in the SOL and between the core and SOL regions.

Acknowledgments

The authors would like to thank Dr. Laura Galeotti for providing the FRC equilibrium data. This work was supported by TAE Grant No. TAE-200441 and US DOE SciDAC ISEP center. Simulations used resources on the Oak Ridge Leadership Computing Facility at Oak Ridge National Laboratory (DOE Contract No. DE-AC05-00OR22725) and the National Energy Research Scientific Computing Center (DOE Contract No. DE-AC02-05CH11231).

ORCID iDs

X.S. Wei  <https://orcid.org/0000-0001-7486-0407>
 W.H. Wang  <https://orcid.org/0000-0001-8743-0430>
 Z. Lin  <https://orcid.org/0000-0003-2007-8983>

G.J. Choi  <https://orcid.org/0000-0003-0044-1650>

C. Lau  <https://orcid.org/0000-0001-6702-1461>

References

- [1] Tuszewski M. 1988 *Nucl. Fusion* **28** 2033
- [2] Rostoker N., Binderbauer M.W. and Monkhorst H.J. 1997 *Science* **278** 1419
- [3] Binderbauer M.W. et al 2015 *Phys. Plasmas* **22** 056110
- [4] Guo H.Y. et al 2015 *Nat. Commun.* **6** 6897
- [5] Gota H. et al 2017 *Nucl. Fusion* **57** 116021
- [6] Gota H. et al 2019 *Nucl. Fusion* **59** 112009
- [7] Schmitz L. et al 2016 *Nat. Commun.* **7** 13860
- [8] Lin Z., Hahm T.S., Lee W.W., Tang W.M. and White R.B. 1998 *Science* **281** 1835
- [9] Fulton D.P., Lau C.K., Schmitz L., Holod I., Lin Z., Tajima T. and Binderbauer M.W. 2016 *Phys. Plasmas* **23** 056111
- [10] Fulton D.P., Lau C.K., Holod I., Lin Z. and Dettrick S. 2016 *Phys. Plasmas* **23** 012509
- [11] Lau C.K., Fulton D.P., Holod I., Lin Z., Binderbauer M., Tajima T. and Schmitz L. 2017 *Phys. Plasmas* **24** 082512
- [12] Lau C.K., Fulton D.P., Bao J., Lin Z., Dettrick S., Binderbauer M., Tajima T. and Schmitz L. 2020 *Phys. Plasmas* **27** 082504
- [13] Lau C.K., Fulton D.P., Bao J., Lin Z., Tajima T., Schmitz L. and Dettrick S. 2019 *Nucl. Fusion* **59** 066018
- [14] Bao J., Lau C.K., Lin Z., Wang H.Y., Fulton D.P., Dettrick S. and Tajima T. 2019 *Phys. Plasmas* **26** 042506
- [15] Wang H.Y. et al 2021 *Plasma Phys. Control. Fusion* **63** 065001
- [16] Hasegawa A. and Mima K. 1977 *Phys. Fluids* **21** 87
- [17] Hasegawa A. and Wakatani M. 1987 *Phys. Rev. Lett.* **59** 1581
- [18] Dimits A.M. et al 2000 *Phys. Plasmas* **7** 969
- [19] Diamond P.H., Itoh S.-I., Itoh K. and Hahm T.S. 2005 *Plasma Phys. Control. Fusion* **47** R35
- [20] Kishimoto Y., Tajima T., Horton W., LeBrun M.J. and Kim J.Y. 1996 *Phys. Plasmas* **3** 1289
- [21] Rosenbluth M.N. and Hinton F.L. 1998 *Phys. Rev. Lett.* **80** 724
- [22] Lin Z., Hahm T.S., Lee W.W., Tang W.M. and Diamond P.H. 1999 *Phys. Rev. Lett.* **83** 3645
- [23] Hinton F.L. and Rosenbluth M.N. 1999 *Plasma Phys. Control. Fusion* **41** A653
- [24] Chen L., Lin Z. and White R. 2000 *Phys. Plasmas* **7** 3129
- [25] Kaye S.M., Gerhardt S., Guttenfelder W., Maingi R., Bell R.E., Diallo A., LeBlanc B.P. and Podesta M. 2013 *Nucl. Fusion* **53** 063005
- [26] Parker S.E. and Lee W.W. 1993 *Phys. Fluids B* **5** 77
- [27] Dimits A.M. and Lee W.W. 1993 *J. Comput. Phys.* **107** 309
- [28] Hu G. and Krommes J.A. 1994 *Phys. Plasmas* **1** 863
- [29] Tajima T. 1989 *Computational Plasma Physics: With Applications To Fusion and Astrophysics* (Reading, MA: Addison-Wesley)
- [30] Lee W.W. 1987 *J. Comput. Phys.* **72** 243
- [31] Lin Z. and Lee W.W. 1995 *Phys. Rev. E* **52** 5646
- [32] Lin Z., Tang W.M. and Lee W.W. 1995 *Phys. Plasmas* **2** 2975
- [33] Shanny R., Dawson J.M. and Greene J.M. 1967 *Phys. Fluids* **10** 1281
- [34] Galeotti L., Barnes D.C., Ceccherini F. and Pegoraro F. 2011 *Phys. Plasmas* **18** 082509
- [35] Xiao Y., Holod I., Wang Z., Lin Z. and Zhang T. 2015 *Phys. Plasmas* **22** 022516
- [36] Lin Z. and Hahm T.S. 2004 *Phys. Plasmas* **11** 1099
- [37] Horton W., Choi D.-I. and Tang W.M. 1981 *Phys. Fluids* **24** 1077
- [38] Hegna C.C., Terry P.W. and Faber B.J. 2018 *Phys. Plasmas* **25** 022511
- [39] Hahm T.S., Beer M.A., Lin Z., Hammett G.W., Lee W.W. and Tang W.M. 1999 *Phys. Plasmas* **6** 922
- [40] Makwana K.D., Terry P.W. and Kim J.-H. 2012 *Phys. Plasmas* **19** 062310